

ARTICLE

Received 18 Feb 2013 | Accepted 5 Jul 2013 | Published 1 Aug 2013

DOI: 10.1038/ncomms3266

Octapod iron oxide nanoparticles as high-performance T_2 contrast agents for magnetic resonance imaging

Zhenghuan Zhao¹, Zijian Zhou¹, Jianfeng Bao², Zhenyu Wang², Juan Hu¹, Xiaoqin Chi³, Kaiyuan Ni¹, Ruifang Wang², Xiaoyuan Chen⁴, Zhong Chen² & Jinhao Gao^{1,5}

Spherical superparamagnetic iron oxide nanoparticles have been developed as T_2 -negative contrast agents for magnetic resonance imaging in clinical use because of their biocompatibility and ease of synthesis; however, they exhibit relatively low transverse relaxivity. Here we report a new strategy to achieve high transverse relaxivity by controlling the morphology of iron oxide nanoparticles. We successfully fabricate size-controllable octapod iron oxide nanoparticles by introducing chloride anions. The octapod iron oxide nanoparticles (edge length of 30 nm) exhibit an ultrahigh transverse relaxivity value ($679.3 \pm 30 \text{ mM}^{-1} \text{ s}^{-1}$), indicating that these octapod iron oxide nanoparticles are much more effective T_2 contrast agents for *in vivo* imaging and small tumour detection in comparison with conventional iron oxide nanoparticles, which holds great promise for highly sensitive, early stage and accurate detection of cancer in the clinic.

¹State Key Laboratory of Physical Chemistry of Solid Surfaces, The Key Laboratory for Chemical Biology of Fujian Province, and Department of Chemical Biology, College of Chemistry and Chemical Engineering, Xiamen University, Xiamen 361005, China. ²Department of Physics and Electronic Science, Fujian Key Laboratory of Plasma and Magnetic Resonance, Xiamen University, Xiamen 361005, China. ³Fujian Provincial Key Laboratory of Chronic Liver Disease and Hepatocellular Carcinoma, Zhongshan Hospital, Xiamen University, Xiamen 361004, China. ⁴Laboratory of Molecular Imaging and Nanomedicine, National Institute of Biomedical Imaging and Bioengineering, National Institutes of Health, Bethesda, Maryland 20892, USA. ⁵Center for Molecular Imaging and Translational Medicine, School of Public Health, Xiamen University, Xiamen 361005, China. Correspondence and requests for materials should be addressed to J.G. (email: jhgao@xmu.edu.cn).

Magnetic resonance imaging (MRI) has a critically important role in molecular imaging and clinical diagnosis, because it is non-invasive and is capable of producing images with high spatial and temporal resolution^{1–3}. Approximately 35% of clinical MR scans need contrast agents to improve their sensitivity and diagnostic accuracy⁴. For example, superparamagnetic iron oxide nanoparticles are the prevailing T_2 contrast agents, especially for the imaging and detection of lesions in normal tissues^{5–8}. However, there are several challenges for using T_2 contrast agents (for example, Feridex and Resovist) in the clinic. As they are intrinsically negative contrast agents, false-positive diagnosis may be found in the hypointense areas, such as blood pooling, calcification and metal deposition^{9–11}. In particular, these commercially available T_2 contrast agents were synthesized in aqueous media and, consequently, exhibit poor crystallinity and relatively low relaxivity¹². Thus, the primary limitation of MRI is the relatively low sensitivity of the contrast agents^{13,14}. The development of new T_2 contrast agents with high relaxivity for high-performance MRI diagnosis is required. Considering that the ability of iron oxide nanoparticles for MRI applications is strongly dependent on their sizes and magnetic characteristics, strategies for making iron oxide nanoparticles based on size control and metal doping have been developed^{15–18}. Usually, the larger spherical iron oxide nanoparticles have stronger saturated magnetization (M_s) and higher T_2 relaxivity (r_2). However, the spherical iron oxide nanoparticles with large size would show ferri/ferromagnetic properties at room temperature, resulting in interparticle agglomeration even in the absence of external magnetic field¹². On the basis of the quantum mechanical outer sphere theory, the T_2 relaxivity is highly dependent on both the M_s value and the effective radius of typically superparamagnetic core^{19–21}. In the motional average regime^{22,23}, the relaxivity r_2 is given by (where all of the nanoparticle contrast agents were simulated as spheres)²⁴

$$r_2 = (256\pi^2\gamma^2/405)\kappa M_s^2 r^2 / D(1 + L/r) \quad (1)$$

where M_s and r are saturation magnetization and effective radius of magnetic nanostructure, respectively, D is the diffusivity of water molecules, L is the thickness of an impermeable surface

coating, and κ is the conversion factor ($\kappa = V^*/C_{Fe}$, V^* is the volume fraction, C_{Fe} is the concentration of Fe element; for more details, see Supplementary Note 1). According to equation (1), we can predict that an increased M_s value or larger effective magnetic core radius will result in a higher r_2 value. Although maintaining the M_s value (the maximum M_s of bulk magnetite is about 92 emu g^{-1} at room temperature), one can still further achieve a much higher T_2 relaxivity by increasing the effective radius of the magnetic core, which is largely morphology dependent.

In the past two decades, controlled synthesis (for example, ion-assisted methods) of unusual and sophisticated metallic nanostructures (for example, octahedral, tetrahedral and concave)^{25–29} is prevailing compared with that of metal oxide nanostructures^{30–32}. However, the investigation of iron oxide nanoparticles with different morphologies is rare, probably because it is difficult to prepare iron oxide nanoparticles with diverse shapes. The nanostructure-activity relationship of iron oxide nanoparticles as MRI contrast agents has not been extensively exploited^{33,34}. Herein, we report a novel strategy to strongly increase T_2 relaxivity by tuning the effective magnetic core radius through morphology control. We successfully synthesize octapod-shaped iron oxide nanoparticles by introducing chloride ions in the reaction system under thermal decomposition conditions. The octapod iron oxide nanoparticles (edge length of 30 nm) exhibit relatively moderate M_s ($\sim 71 \text{ emu g}^{-1}$) but ultrahigh r_2 relaxivity ($679.3 \pm 30 \text{ mM}^{-1} \text{ s}^{-1}$) because of the unique structure and highly effective boundary radius. The animal study shows that the octapod iron oxide nanoparticles are suitable as high-performance T_2 contrast agents for *in vivo* MRI and early tumour detection, particularly for liver lesions.

Results

Synthesis and characterization. The octapod iron oxide nanoparticles were prepared via decomposition of iron oleate in the presence of sodium chloride (NaCl). Briefly, the iron oleate was decomposed at 320°C for 2 h in 1-octadecene solvent containing oleic acid as the surfactant and NaCl as the capping agent. Transmission electron microscopy (TEM) images (Fig. 1a,b) showed that the as-prepared product consists of uniform four-

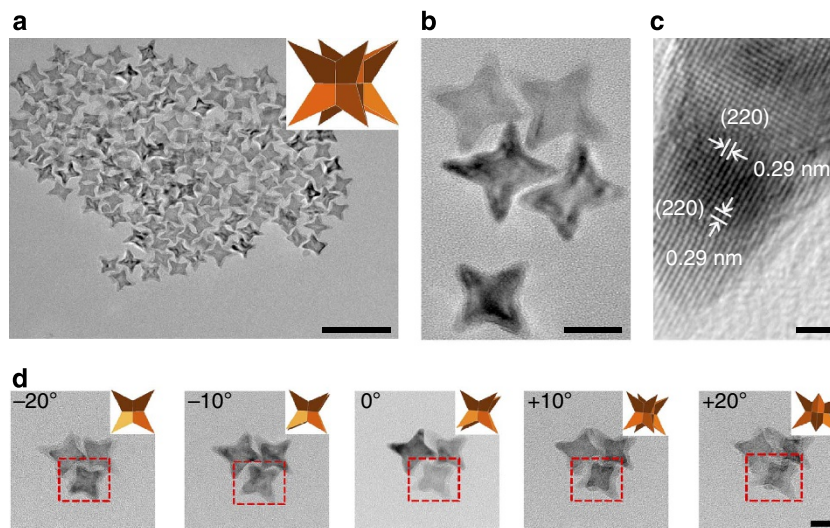


Figure 1 | TEM analyses of octapod iron oxide nanoparticles. (a) TEM image of Octapod-30 consisted of uniform four-armed star-like particles (inset: geometric model). Scale bar, 100 nm. (b) The higher magnification TEM image of Octapod-30. Scale bar, 20 nm. (c) high-resolution TEM image of Octapod-30, showing the single crystallinity with the lattice fringes across the entire nanoparticles correspond to Fe_3O_4 (220). Scale bar, 2 nm. (d) Tilted TEM images of three Octapod-30. Along with the tilting, the nanoparticles (red dotted squares) change from four-armed star-like to elongated six-armed stars, indicating that the geometric shape of Octapod-30 is a concave octapod owning eight trigonal pyramidal arms (insets: corresponding geometric models). Scale bar, 20 nm.

armed star-like iron oxide particles with high yield (>95%). The average edge length between two nearby armed points is about 30 nm. We observed uniform lattice fringes across the entire nanoparticles with spacing corresponding to Fe_3O_4 (220) in high-resolution TEM images (Fig. 1c). After carefully surveying these unique nanoparticles, we found some shadows likely belong to the four arms of star-like particles, indicating the possible presence of concave feature in the particles. To better visualize the three-dimensional structure of the nanoparticles, we tilted the sample away from the direction perpendicular to the electron beam. Along with the tilting, the nanoparticles changes from four-armed star-like to elongated six-armed stars (Fig. 1d), which fits to the feature of octapod nanoparticles owning eight trigonal pyramidal arms²⁷. On the basis of these observations, we proposed a concave polyhedral model of this unique iron oxide nanostructure (Fig. 1a, inset). To confirm this proposed structure, we characterized an individual octapod nanoparticle by high-resolution TEM and relevant selected-area electron diffraction measurements. Both the outlines and angles between the edges of individual nanoparticle are consistent with the geometric models of concave bounded by [311] high-index facets (Supplementary Fig. S1). The X-ray powder diffraction pattern of octapod nanoparticles matched well with magnetite Fe_3O_4 reference values (JCPDS number 82-1533) without any iron phase, suggesting the octapod iron oxide nanoparticles are pure magnetite with inversed spinel crystal structure (Supplementary Fig. S2).

Controlled synthesis of octapod iron oxide nanoparticles. As expected, NaCl may be essential in the synthesis of octapod iron oxide nanoparticles. We obtained the uniform octapod iron oxide nanoparticles by supplying a certain amount of NaCl (0.17 mmol of NaCl to 0.86 mmol of iron oleate) to a 10 ml of reaction solution. When the amount of NaCl was reduced to 0.085 mmol, the yield of octapod iron oxide nanoparticles was significantly reduced. There were very few octapod iron oxide nanoparticles when the amount of NaCl was further decreased to 0.034 mmol (Supplementary Fig. S3). These results suggest that NaCl may have an important role in the formation of octapod iron oxide nanoparticles. To understand the effects of chloride anions and sodium cations in the formation of octapod iron oxide nanoparticles, we conducted a number of control experiments. When using NaOH and Na oleate instead of NaCl, the products were mainly the mixture of spherical and cubic iron oxide nanoparticles. Similarly, we did not obtain the octapod structure after adding either NaF or KBr in reactions (Supplementary Fig. S4), indicating that the chloride ions are more critical in the formation of octapod iron oxide nanoparticles than of sodium ions. Furthermore, we used hexadecyl trimethyl ammonium chloride, KCl, hexadecyl trimethyl ammonium bromide and KBr instead of NaCl to investigate the structures of final products (Supplementary Fig. S5). The similar octapod products were obtained by adding hexadecyl trimethyl ammonium chloride or KCl, whereas no desired octapod structures were obtained in the presence of hexadecyl trimethyl ammonium bromide or KBr. These results further confirm that the chloride ions are the key inducer of the formation of octapod iron oxide nanoparticles. We were also able to control the sizes of octapod nanoparticles by varying the reaction time in the presence of NaCl. The octapod nanoparticles with average edge lengths of 14, 20, 30 and 36 nm were formed by reaction for 0.5, 1, 2 and 2.5 h, respectively (Fig. 2a–d), suggesting that the chloride ions may affect the formation of octapod nanoparticles throughout the particle growth process. One possible mechanism of forming octapod iron oxide nanoparticles was that the chloride ions were selectively bound to

iron ions exposed on the high-index facets (probably [311]) of iron oxide during the particle growth (Fig. 2e,f). Such a chloride ion-assisted formation mechanism was supported by finding the presence of a trace amount of chlorine on the octapod iron oxide nanoparticles using energy-dispersive X-ray spectroscopy and X-ray photoelectron spectroscopy (Fig. 2e and Supplementary Fig. S6). To the best of our knowledge, this is the first report on the controlled synthesis of unique octapod iron oxide nanostructures with high surface-to-volume ratio (Supplementary Note 2).

Structure and properties of octapod iron oxide nanoparticles.

Sophisticated morphology of nanostructures may alter the effective radii of particle cores. According to the quantum mechanical outer sphere theory, we simulated a spherical ball covering the full octapod iron oxide nanoparticle as a model to represent the objective existence of octapod nanoparticles under an external magnetic field B_0 (Fig. 3a). Thus, the diameter of the model shows the effective diameters of octapod iron oxide nanoparticles. We found the effective radii of octapod iron oxide nanoparticles to be ~ 2.4 times as large as that of spherical nanoparticles having the same geometric core volumes (Supplementary Fig. S7 and Supplementary Note 2), demonstrating that the octapod morphology can significantly increase the effective radii of nanoparticles and indicating that octapod iron oxide nanoparticles may possess much higher T_2 relaxivity than the spherical nanoparticles with similar geometric volumes. To investigate the MRI contrast ability of octapod and spherical iron oxide nanoparticles with the same geometric volumes, we chose the octapod iron oxide nanoparticles with average edge lengths of 30 nm (denoted as Octapod-30) and 20 nm (denoted as Octapod-20) as two representative examples. Accordingly, spherical nanoparticles with mean diameters of 16 nm (denoted as Spherical-16) and 10 nm (denoted as Spherical-10) were used for comparison because of the similarity in volume (that is, Octapod-30 with Spherical-16 and Octapod-20 with Spherical-10). We then tested the magnetic properties of octapod and spherical iron oxide nanoparticles by a superconducting quantum interference device. Octapod-30, Octapod-20, Spherical-16 and Spherical-10 all showed a smooth $M-H$ curve with no hysteresis at ambient temperature (Fig. 3b). The blocking temperature of Octapod-30 and Octapod-20 were 290 K and 240 K, respectively (Supplementary Fig. S8), which further confirmed that Octapod-30 and Octapod-20 exhibited superparamagnetic behaviours at room temperature, enabling these nanoparticles for many biomedical applications (for example, biological separation and MRI contrast enhancement). The M_s values of Octapod-30, Octapod-20, Spherical-16 and Spherical-10 were about 71, 51, 67 and 55 emu g^{-1} , respectively. The slightly higher M_s value of Octapod-30 than that of Spherical-16 may be due to the reduced spin canting effect in octapod morphology comparing with spherical particle³⁵. Despite of similar M_s values, the shape anisotropy in these octapod magnetite nanostructures and significantly increased effective radii of the magnetic cores may be responsible for the distinctly high T_2 relaxivities.

As the as-prepared nanoparticles were hydrophobic and unsuitable for biomedical applications, we transferred the nanoparticles to aqueous media using the conjugates of dendritic molecules and 1-hexadecylamine (denoted as HDA- G_2) by a hydrophobic–hydrophobic interaction³⁶. The encapsulated nanoparticles showed excellent colloidal stability in aqueous solution. We did not observe any aggregations or morphology alteration after storage for more than 1 month (Supplementary Fig. S9). Furthermore, we measured the hydrodynamic diameters (HDs) of all the samples by dynamic light scattering. The HDs of

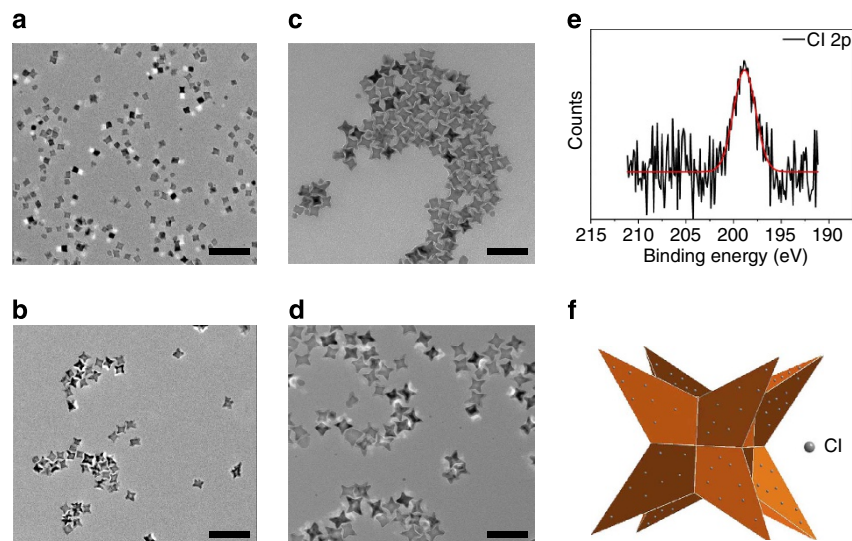


Figure 2 | Controlled synthesis of octapod iron oxide nanoparticles with different edge lengths. The octapod iron oxide nanoparticles with edge lengths of (a) 14, (b) 20, (c) 30 and (d) 36 nm formed after 1, 1.5, 2 and 2.5 h reaction times in the presence of NaCl, respectively. (e) X-ray photoelectron spectroscopy analysis of octapod iron oxide nanoparticles showed the Cl 2p_{3/2} peak at 198.9 eV, corresponding to the binding energy of Cl-Fe(III). The red line is a fitted result of the spectrum. (f) The model illustrated that the Cl ions may selectively bind to Fe ions on the surface of octapod iron oxide nanoparticles during size growth. Scale bar, 100 nm.

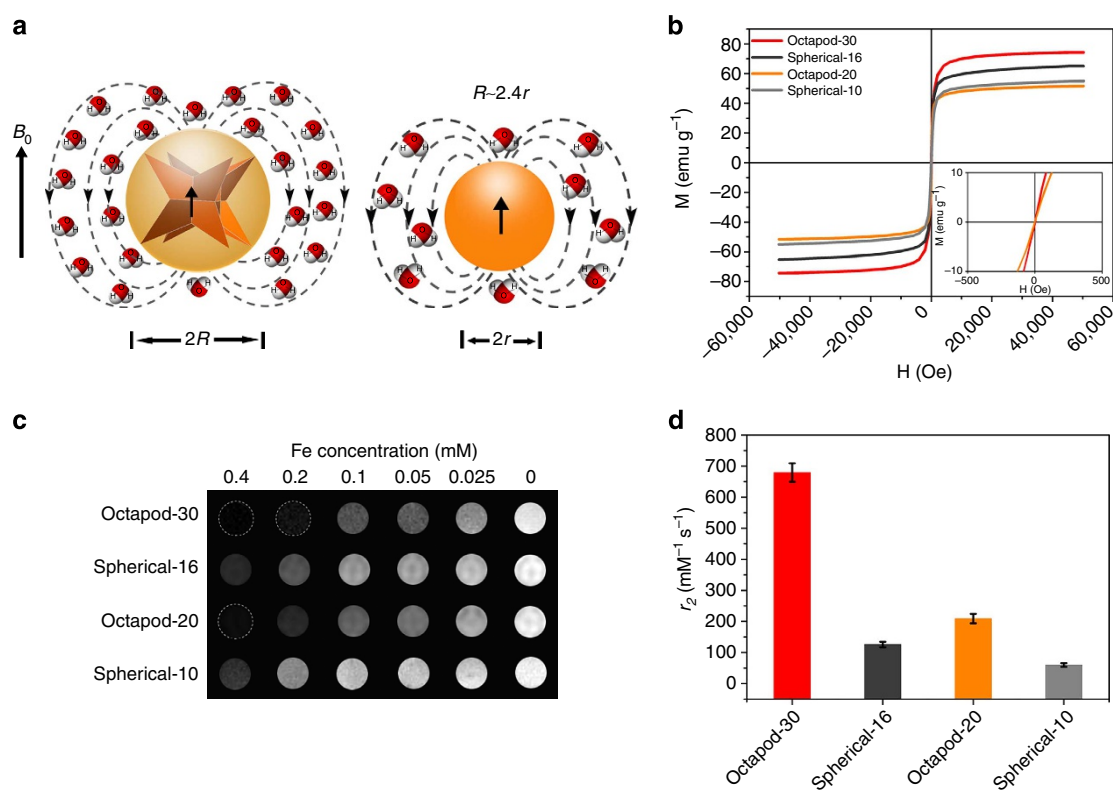


Figure 3 | MR contrast effect of octapod iron oxide nanoparticles. (a) Schematic cartoon shows the ball models of octapod and spherical iron oxide nanoparticles with the same geometric volume (the black dotted lines represents the magnetic field of the octapod and spherical iron oxide nanoparticles. The same length of black arrow means the same M_s of octapod and spherical iron oxide nanoparticles). With the same geometric core volume, the octapod nanoparticles have much larger effective volume (radius, R) than the spherical nanoparticles (radius, r) with $R \sim 2.4r$ under an external magnetic field B_0 . (b) The smooth $M-H$ curves of Octapod-30, Octapod-20, Spherical-16 and Spherical-10 measured at 300 K using a superconducting quantum interference device magnetometer (inset: $M-H$ curves of Octapod-30 and Octapod-20 in low-magnetic field areas). The M_s values of Octapod-30, Octapod-20, Spherical-16 and Spherical-10 are about 71, 51, 67 and 55 $\mu\text{m g}^{-1}$, respectively. (c) T_2 -weighted MR images of Octapod-30, Octapod-20, Spherical-16 and Spherical-10 in aqueous solution with 1% agarose at various concentrations of iron using a Varian 7T microMRI scanner. (d) Comparison of r_2 values of Octapod-30, Octapod-20, Spherical-16 and Spherical-10. The error bars represent \pm s.d. of five independent experiments.

Spherical-10, Spherical-16, Octapod-20 and Octapod-30 were 22 ± 2 , 30 ± 3 , 49 ± 5 and 58 ± 2 nm, respectively (Supplementary Fig. S9), suggesting that the iron oxide nanoparticles were monodisperse in water without any clustering and aggregation. Moreover, there are a large number of free amine groups available on the surface of the water-dispersible octapod nanoparticles, allowing for further modification and functionalization. It is of note that the HD of Octapod-30 is about twice as much as that of Spherical-16, which is consistent with the proposed model (Fig. 3a). In addition, the physical surface-to-volume ratio of Octapod-30 in aqueous medium is larger than that of the simulated spherical model because of the unique octapod structure. Hence, it is expected that the effective surface area of Octapod-30 for diffusion of water molecules may be more than four times greater than that of Spherical-16.

Transverse relaxivity of octapod iron oxide nanoparticles. We then tested the transverse relaxivity (r_2) values of the above four samples by a 7T MR scanner. With the increase of Fe concentrations, the signal intensity of T_2 -weighted phantom images obviously decreased (Fig. 3c), indicating that all the samples have the potential to generate MRI contrast enhancement on T_2 -weighted sequences. Notably, the octapod iron oxide nanoparticles exhibited stronger T_2 contrast effects than spherical iron oxide nanoparticles, suggesting that the octapod iron oxide nanoparticles may serve as highly sensitive T_2 contrast agents. The r_2 values of Octapod-30, Octapod-20, Spherical-16 and Spherical-10 were about 679.25 ± 30 , 209.03 ± 15 , 125.86 ± 9 and 59.91 ± 6 $\text{mM}^{-1} \text{s}^{-1}$, respectively (Fig. 3d and Supplementary Figs S10 and S11). Because of the increased effective radii of octapod iron oxide cores, the r_2 value of Octapod-30 was ~ 5.4 times larger than that of Spherical-16. Meanwhile, Octapod-20 has a higher r_2 value than Spherical-10 (about 3.5 times) as well. It should be mentioned that the M_s values and geometric volumes of both octapod iron oxide nanoparticles were very close to the corresponding spherical iron oxide nanoparticles (that is, Octapod-30 to Spherical-16 and Octapod-20 to Spherical-10). Our results demonstrate that structurally increasing the effective radii of iron oxide through morphology control is an attractive alternative to existing strategies, such as metal doping and particle clustering^{18,37–39} to increase the T_2 relaxivity of iron oxide nanoparticles.

Liver MRI using octapod iron oxide nanoparticles. Iron oxide nanoparticles as T_2 contrast agents have been extensively used in liver MRI. Before the animal study, we first tested the cytotoxicity of water-dispersible octapod iron oxide nanoparticles using HepG2 cell line as a model. The MTT (3-(4,5-dimethylthiazol-2-yl)-2,5-diphenyltetrazolium bromide) assay indicated that octapod iron oxide nanoparticles have no appreciable cytotoxicity for 24 h even at concentration up to 100 μg Fe per ml, suggesting the high biocompatibility of the octapod iron oxide nanoparticles (Supplementary Fig. S12). To verify that octapod iron oxide nanoparticles display better contrast effects than traditional spherical iron oxide nanoparticles *in vivo*, we chose Octapod-30 and Spherical-16 as representative samples and conducted T_2 -weighted MRI of liver using BALB/c mouse as a model. After intravenous injection of Octapod-30 and Spherical-16 samples at a dose of 1 mg Fe per kg of mouse body weight, we indeed observed significant signal attenuation in the liver region for both nanoparticles (Fig. 4a) at 0.5 h post injection (p.i.). To quantify the contrast, we identified the liver as the region of interest and calculated the signal-to-noise ratio (SNR) and $\text{SNR}_{\text{post}}/\text{SNR}_{\text{pre}}$ value for each animal (Fig. 4b and Supplementary Table S1). It appears that the Octapod-30 exhibited much higher contrast

(63.9 ± 3.2 and $67.3 \pm 1.3\%$ at 0.5 and 1 h p.i., respectively) than Spherical-16 (39.8 ± 1.5 and $53.5 \pm 1.6\%$ at 0.5 and 1 h p.i., respectively), suggesting that Octapod-30 with higher r_2 value is more sensitive than Spherical-16 in T_2 imaging of liver *in vivo*. Prussian blue staining detected blue spots throughout the liver sections after administration of Octapod-30 and Spherical-16 (Supplementary Fig. S13), confirming that the signal attenuation in the liver was caused by iron oxide nanoparticle accumulation. The inductively coupled plasma mass spectrometry analysis (Supplementary Fig. S14) indicates that the liver uptake of Octapod-30 and Spherical-16 is in a comparable manner, demonstrating that the much better contrast is due to the higher r_2 value of Octapod-30. In MRI, lower dose of contrast agents may imply lower cost and less side effect, which pledges greater prospects in clinical diagnosis. The high contrast of Octapod-30 prompted us to conduct liver MRI at a lower dose. By reducing the injection dose of Octapod-30 to 0.5 mg Fe per kg, the contrast ($39.9 \pm 2.5\%$ at 0.5 h and $56.2 \pm 1.9\%$ at 1 h) was still slightly higher than that when Spherical-16 at 1 mg kg^{-1} does (Supplementary Fig. S15 and Supplementary Table S1).

Detection of liver cancer by MRI. To further evaluate the ability of Octapod-30 for liver cancer imaging, we conducted a T_2 -weighted MRI on an orthotopic HepG2 tumour model. We established the orthotopic liver tumour model by inoculation of small subcutaneous HepG2 tumour fragments into the liver of nude mice. When the hepatic carcinoma reached 3–5 mm in diameter, we intravenously injected Octapod-30 and Spherical-16 into the nude mice (2 mg Fe per kg) and scanned the animals at a 7T microMRI scanner. As hepatic tumours contain much less active Kupffer cells and macrophages³⁶, they do not accumulate iron oxide nanoparticles as efficiently as normal liver tissues do^{40,41}. Thus, the hepatic tumours would show pseudo-positive contrast as compared with normal liver tissues. Both particles caused obvious contrast enhancement in the tumour sites after intravenous administration (Fig. 4c). Moreover, the injection of Octapod-30 resulted in higher MR contrast in the tumour site than Spherical-16, leading to easy differentiation between the liver lesions and normal liver tissues in the MR images. The tumour-to-liver contrast increased over time and was as high as 136.9 ± 8.5 and $64.5 \pm 2.7\%$ at 4 h p.i. for Octapod-30 and Spherical-16, respectively (Fig. 4d and Supplementary Table S2), indicating that Octapod-30 exhibited much higher signal changes for liver tumour imaging and detection limit than Spherical-16. The use of Octapod-30 with ultrahigh T_2 relaxivity as contrast agent may significantly improve the sensitivity of T_2 imaging, which should be extremely important for accurate detection and early diagnosis of cancer.

Discussion

We further compared the r_2 values of spherical nanoparticles with mean diameter of 25 nm (donated as Spherical-25) and Octapod-20, which have the similar effective diameters (HDs). The results demonstrated that the r_2 value of Octapod-20 is somewhat higher than that of Spherical-25, although the M_s value of Spherical-25 is larger than that of Octapod-20 (Supplementary Fig. S11). This phenomenon may be attributed to the strong inhomogeneity of the local magnetic fields induced by the unique octapod-shaped iron oxide nanoparticles, suggesting that the outer sphere theory may have limitations when applied to nanoparticles with significant anisotropy²¹. Because of the unique morphology of octapod iron oxide nanoparticles, the local magnetic field induced by an octapod iron oxide nanoparticle under an external magnetic field (B_0) may be more inhomogeneous than that of a spherical one, which may further induce proton dephasing and

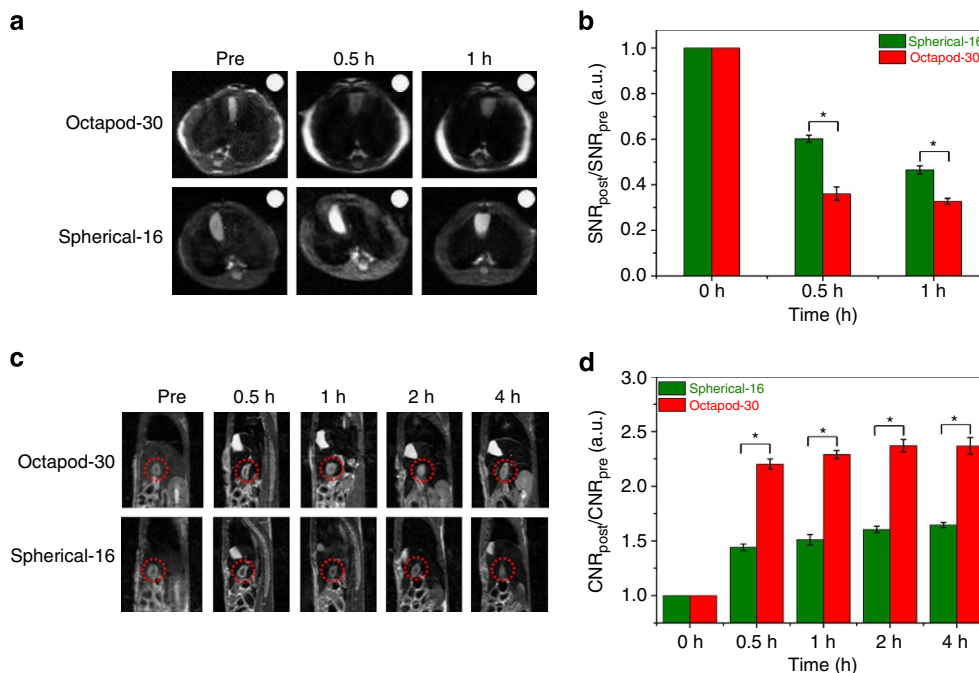


Figure 4 | *In vivo* MRI. (a) *In vivo* MR images of BALB/c mice at 0, 0.5 and 1 h after intravenous injection of Octapod-30 (upper) and Spherical-16 (lower) in transverse plane, respectively (the white dot is the signal reference using water in an NMR tube). (b) Quantification of liver contrast collected at 0, 0.5 and 1 h after accumulation of Octapod-30 and Spherical-16 in BALB/c mice at dose of 1.0 mg Fe per kg, respectively ($*P < 0.01$). (c) *In vivo* MR images of orthotopic xenograft liver tumour model at 0, 0.5, 1, 2 and 4 h after intravenous injection of Octapod-30 and Spherical-16 in sagittal plane. (d) Quantification of contrast-to-noise ratio (CNR) of tumour-to-liver contrast at 0, 0.5, 1, 2 and 4 h after administration of Octapod-30 and Spherical-16, with a dose of 2.0 mg Fe per kg, respectively ($*P < 0.01$).

enhance the T_2 shortening⁴². On the basis of the calculations using the Landau–Lifshitz–Gilbert equation, we found that the octapod morphology did result in a significantly more inhomogeneous induced magnetic field than the spherical one as expected, whereas the induced magnetic field in the far field (micrometer away) is negligible ($\sim 10^{-3}$ Oe) and almost the same regardless of the nanoparticle shape (Supplementary Fig. S16 and Supplementary Table S3). These results indicate that octapod iron oxide nanoparticles could further increase the r_2 value by inducing a more inhomogeneous magnetic field. The fact that the r_2 value of Spherical-25 is close to that of Octapod-20 manifests that the increased effective radius is the main reason to improve the transverse relaxivity of octapod iron oxide nanoparticles.

In summary, we have demonstrated a novel strategy for designing concave octapod iron oxide nanoparticles with ultrahigh r_2 values as T_2 contrast agents. The key to successful fabrication of size-controllable octapod iron oxide nanoparticles is the presence of chloride anions. It turns out that by increasing the effective radius and local field inhomogeneity of the magnetic core, the octapod iron oxide nanoparticles exhibit an incredibly high T_2 contrast enhancement effect. The controlled synthesis of octapod iron oxide nanoparticles is facile, highly reproducible and amenable to scale up, thereby rendering these novel iron oxide nanoparticles promising T_2 contrast agents for MRI. This new strategy of achieving extremely high T_2 relaxivity of iron oxide nanoparticles by increasing the effective radii of iron oxide cores rather than the magnetization values is believed to be critically important in developing highly sensitive second-generation contrast agents for MRI (Supplementary Table S4), especially for the early and accurate diagnosis of liver cancer in patients. Moreover, the controllable synthesis of novel octapod iron oxide nanoparticles, together with other morphologies (for example,

sphere, cube and rod), certainly facilitates the applications of magnetic nanoparticles in high-density data storage, hyperthermia treatment and magnetically guided drug delivery.

Methods

Synthesis of octapod iron oxide nanoparticles. In a typical synthesis of octapod iron oxide nanoparticles, iron oleate (0.8 g, 0.86 mmol), NaCl (10 mg, 0.17 mmol), oleic acid (110 μ l, 0.35 mmol) and distilled water (60 μ l) were mixed together with 10 ml of 1-octadecene. The resulting solution was degassed in vacuum for 30 min and backfilled with argon to remove any low volatile impurities and oxygen at room temperature. And then, we heated the reaction solution to 320 °C with a constant heating rate of 3.3 °C min⁻¹, and were kept at the temperature for 2 h. The colour of the solution changed from reddish-brown to transparent orange and finally brownish-black. Then, the solution was cooled to room temperature and mixed with 30 ml of isopropanol to precipitate the nanoparticles. The nanoparticles were separated by centrifugation and washed three times with ethanol. The final product was dissolved in hexane for long-term storage at 4 °C. See Supplementary Methods for further details of synthesis procedures.

Measurement of T_2 relaxivities. To measure the T_2 relaxivity, Octapod-30, Octapod-20, Spherical-16 and Spherical-10 with different iron concentrations were dispersed in 1% agarose solution. The samples were scanned (at 300 K) using a T_2 -weighted fast spin-echo multi-slice sequence (fSEMS) (TR/TE = 2,000/20, 40, 60, 80, 100 ms, slice thickness = 2 mm) by a 7T MRI scanner (Varian 7T microMRI System).

***In vivo* liver MRI.** Animal experiments were executed according to the protocol approved by Institutional Animal Care and Use Committee of Xiamen University. We performed the *in vivo* MRI of liver by using BALB/c mouse as a model. After intravenous injection of iron oxide nanoparticles at a dose of 1 mg Fe per kg of mouse body weight, the coronal and transverse plane MR images were scanned using an fSEMS (TR/TE = 3,000/40 ms, 256 \times 256 matrices, averages = 1) on a Varian 7T microMRI scanner. The MR images were obtained at pre-injection, 0.5 and 1 h p.i. ($n = 3$ per group). To qualify the signal enhancement, we calculated the SNR by the equation: $SNR_{liver} = SI_{liver}/SD_{noise}$ where SI represents signal intensity and SD represents s.d.

In vivo liver tumour imaging. We established the orthotopic liver tumour model by inoculation of small subcutaneous HepG2 tumour fragments into the liver of nude mice. When the tumour reached 3–5 mm in diameter, mice were intravenously injected with Octapod-30 and Spherical-16 at a dose of 2 mg Fe per kg. The coronal and transverse plane MR images were acquired using an fSEMS (TR/TE = 3,000/40 ms, 256 × 256 matrices, averages = 1) on a 7T MRI scanner. The MR images were sequentially obtained at 0, 0.5, 1, 2 and 4 h p.i. ($n = 3$ per group). To qualify the efficacy of contrast enhancement, we introduced the CNR (contrast-to-noise ratio), which was given by $CNR = (SNR_{\text{tumour}} - SNR_{\text{liver}}) / SNR_{\text{tumour}}$.

References

- Laurent, S. *et al.* Magnetic iron oxide nanoparticles: Synthesis, stabilization, vectorization, physicochemical characterizations, and biological applications. *Chem. Rev.* **108**, 2064–2110 (2008).
- Tassa, C., Shaw, S. Y. & Weissleder, R. Dextran-coated iron oxide nanoparticles: a versatile platform for targeted molecular imaging, molecular diagnostics, and therapy. *Acc. Chem. Res.* **44**, 842–852 (2011).
- Corot, C., Robert, P., Idee, J. M. & Port, M. Recent advances in iron oxide nanocrystal technology for medical imaging. *Adv. Drug Deliv. Rev.* **58**, 1471–1504 (2006).
- Major, J. L. & Meade, T. J. Bioresponsive, cell-penetrating, and multimeric MR contrast agents. *Acc. Chem. Res.* **42**, 893–903 (2009).
- Weissleder, R. *et al.* Ultrasmall superparamagnetic iron oxide - characterization of a new class of contrast agents for MR imaging. *Radiology* **175**, 489–493 (1990).
- Bulte, J. W. M. & Kraitchman, D. L. Iron oxide MR contrast agents for molecular and cellular imaging. *NMR Biomed.* **17**, 484–499 (2004).
- Harisinghani, M. G. *et al.* Noninvasive detection of clinically occult lymph-node metastases in prostate cancer. *N. Engl. J. Med.* **348**, 2491–2495 (2003).
- Gao, J. H., Gu, H. W. & Xu, B. Multifunctional magnetic nanoparticles: design, synthesis, and biomedical applications. *Acc. Chem. Res.* **42**, 1097–1107 (2009).
- Terreno, E., Castelli, D. D., Viale, A. & Aime, S. Challenges for molecular magnetic resonance imaging. *Chem. Rev.* **110**, 3019–3042 (2010).
- Kim, B. H. *et al.* Large-scale synthesis of uniform and extremely small-sized iron oxide nanoparticles for high-resolution T_1 magnetic resonance imaging contrast agents. *J. Am. Chem. Soc.* **133**, 12624–12631 (2011).
- Lee, N. & Hyeon, T. Designed synthesis of uniformly sized iron oxide nanoparticles for efficient magnetic resonance imaging contrast agents. *Chem. Soc. Rev.* **41**, 2575–2589 (2012).
- Lee, N. *et al.* Magnetosome-like ferrimagnetic iron oxide nanocubes for highly sensitive MRI of single cells and transplanted pancreatic islets. *Proc. Natl Acad. Sci. USA* **108**, 2662–2667 (2011).
- Ananta, J. S. *et al.* Geometrical confinement of gadolinium-based contrast agents in nanoporous particles enhances T1 contrast. *Nat. Nanotech.* **5**, 815–821 (2010).
- Ghosh, D. *et al.* M13-templated magnetic nanoparticles for targeted in vivo imaging of prostate cancer. *Nat. Nanotech.* **7**, 677–682 (2012).
- Sun, S. H. & Zeng, H. Size-controlled synthesis of magnetite nanoparticles. *J. Am. Chem. Soc.* **124**, 8204–8205 (2002).
- Park, J. *et al.* Ultra-large-scale syntheses of monodisperse nanocrystals. *Nat. Mater.* **3**, 891–895 (2004).
- Lee, J.-H. *et al.* Artificially engineered magnetic nanoparticles for ultra-sensitive molecular imaging. *Nat. Med.* **13**, 95–99 (2007).
- Jang, J.-t. *et al.* Critical enhancements of MRI contrast and hyperthermic effects by dopant-controlled magnetic nanoparticles. *Angew. Chem. Int. Ed.* **48**, 1234–1238 (2009).
- Yoo, D., Lee, J.-H., Shin, T.-H. & Cheon, J. Theranostic magnetic nanoparticles. *Acc. Chem. Res.* **44**, 863–874 (2011).
- Koenig, S. H. & Kellar, K. E. Theory of $1/T_1$ and $1/T_2$ NMRD profiles of solutions of magnetic nanoparticles. *Magn. Reson. Med.* **34**, 227–233 (1995).
- Roch, A., Muller, R. N. & Gillis, P. Theory of proton relaxation induced by superparamagnetic particles. *J. Chem. Phys.* **110**, 5403–5411 (1999).
- Vuong, Q. L., Berret, J.-F., Fresnais, J., Gossuin, Y. & Sandre, O. A universal scaling law to predict the efficiency of magnetic nanoparticles as MRI T_2 -contrast agents. *Adv. Healthcare Mater.* **1**, 502–512 (2012).
- Gillis, P., Moïny, F. & Brooks, R. A. On T_2 -shortening by strongly magnetized spheres: a partial refocusing model. *Magn. Reson. Med.* **47**, 257–263 (2002).
- Tong, S., Hou, S., Zheng, Z., Zhou, J. & Bao, G. Coating optimization of superparamagnetic iron oxide nanoparticles for high T_2 relaxivity. *Nano Lett.* **10**, 4607–4613 (2010).
- Tian, N., Zhou, Z. Y., Sun, S. G., Ding, Y. & Wang, Z. L. Synthesis of tetrahedral platinum nanocrystals with high-index facets and high electro-oxidation activity. *Science* **316**, 732–735 (2007).
- Lim, B., Xiong, Y. & Xia, Y. A water-based synthesis of octahedral, decahedral, and icosahedral Pd nanocrystals. *Angew. Chem. Int. Ed.* **46**, 9279–9282 (2007).
- Huang, X., Zhao, Z., Fan, J., Tan, Y. & Zheng, N. Amine-assisted synthesis of concave polyhedral platinum nanocrystals having [411] high-index facets. *J. Am. Chem. Soc.* **133**, 4718–4721 (2011).
- Zhang, J. *et al.* Concave cubic gold nanocrystals with high-index facets. *J. Am. Chem. Soc.* **132**, 14012–14014 (2010).
- Huang, X. *et al.* Freestanding palladium nanosheets with plasmonic and catalytic properties. *Nat. Nanotech.* **6**, 28–32 (2011).
- Yin, J. *et al.* Low-symmetry iron oxide nanocrystals bound by high-index facets. *Angew. Chem. Int. Ed.* **49**, 6328–6332 (2010).
- Hofmann, C. *et al.* Shape control of new $\text{Fe}_x\text{O}-\text{Fe}_3\text{O}_4$ and $\text{Fe}_{1-y}\text{Mn}_y\text{O}-\text{Fe}_3\text{O}_4$ nanostructures. *Adv. Funct. Mater.* **18**, 1661–1667 (2008).
- Hou, Y. L., Xu, Z. C. & Sun, S. H. Controlled synthesis and chemical conversions of FeO nanoparticles. *Angew. Chem. Int. Ed.* **46**, 6329–6332 (2007).
- Zabow, G., Dodd, S., Moreland, J. & Koretsky, A. Micro-engineered local field control for high-sensitivity multispectral MRI. *Nature* **453**, 1058–1063 (2008).
- Zabow, G., Dodd, S. J., Moreland, J. & Koretsky, A. P. The fabrication of uniform cylindrical nanoshells and their use as spectrally tunable MRI contrast agents. *Nanotechnology* **20**, 385301 (2009).
- Noh, S.-H. *et al.* Nanoscale magnetism control via surface and exchange anisotropy for optimized ferrimagnetic hysteresis. *Nano Lett.* **12**, 3716–3721 (2012).
- Zhou, Z. J. *et al.* A synergistically enhanced T_1 - T_2 dual-modal contrast agent. *Adv. Mater.* **24**, 6223–6228 (2012).
- Ai, H. *et al.* Magnetite-loaded polymeric micelles as ultrasensitive magnetic-resonance probes. *Adv. Mater.* **17**, 1949–1952 (2005).
- Bruns, O. T. *et al.* Real-time magnetic resonance imaging and quantification of lipoprotein metabolism in vivo using nanocrystals. *Nat. Nanotech.* **4**, 193–201 (2009).
- Yoon, T.-J., Lee, H., Shao, H. & Weissleder, R. Highly magnetic core-shell nanoparticles with a unique magnetization mechanism. *Angew. Chem. Int. Ed.* **50**, 4663–4666 (2011).
- Huang, J. *et al.* Effects of nanoparticle size on cellular uptake and liver MRI with polyvinylpyrrolidone-coated iron oxide nanoparticles. *ACS Nano* **4**, 7151–7160 (2010).
- Ba-Ssalamah, A. *et al.* Clinical value of MRI liver-specific contrast agents: a tailored examination for a confident non-invasive diagnosis of focal liver lesions. *Eur. Radiol.* **19**, 342–357 (2009).
- Bjørnerud, A. & Johansson, L. The utility of superparamagnetic contrast agents in MRI: theoretical consideration and applications in the cardiovascular system. *NMR Biomed.* **17**, 465–477 (2004).

Acknowledgements

This work was supported by the National Key Basic Research Program of China (2013CB933901 and 2013CB733802), National Natural Science Foundation of China (21222106, 21021061, 81000662, 81201805 and J1210014), Natural Science Foundation of Fujian (2013J06005) and the Program for New Century Excellent Talents in University (NCET-10-0709). We thank B. Xu, L.S. Zheng, E. Meggers and C.B. Cai for the fruitful discussions.

Author contributions

J.G. and Z. Zhao conceived and designed the experiments; Z. Zhao, Z. Zhou, J.B., J.H., X. Chi. and K.N. performed the experiments; J.G., Z. Zhao and Z.C. analysed the data; Z.W. and R.W. did the theoretical calculations; and J.G., X. Chen and Z. Zhao co-wrote the paper. All authors discussed the results and commented on the manuscript.

Additional information

Supplementary Information accompanies this paper at <http://www.nature.com/naturecommunications>

Competing financial interests: The authors declare no competing financial interests.

Reprints and permission information is available online at <http://npg.nature.com/reprintsandpermissions/>

How to cite this article: Zhao, Z. *et al.* Octapod iron oxide nanoparticles as high-performance T_2 contrast agents for magnetic resonance imaging. *Nat. Commun.* **4**:2266 doi: 10.1038/ncomms3266 (2013).